Nano Research

Open Access

Research Article

First-principles insight into helical distortion in chiral WSe_2 for promoting C–C coupling in CO_2 reduction

Tianwei Ouyang[1], Hang Su[2], Shunai Che[1] ✉, and Yuxi Fang[1] ✉

[1] *State Key Laboratory of Synergistic Chem-Bio Synthesis, School of Chemistry and Chemical Engineering, Frontiers Science Center for Transformative Molecules, Shanghai Key Laboratory for Molecular Engineering of Chiral Drugs, Shanghai Jiao Tong University, Shanghai 200240, China*

[2] *Institute of Condensed Matter Physics, School of Physics and Astronomy, Shanghai Jiao Tong University, Shanghai 200240, China*

Cite this article: *Nano Research*, **2026**, *19*, 94908369. https://doi.org/10.26599/NR.2026.94908369

ABSTRACT: Catalytic conversion of CO_2 into multi-carbon products represents a promising route for sustainable carbon utilization, yet its practical realization remains limited by the high energy barrier associated with C–C coupling. Here, we demonstrate that the out-of-plane helical distortion in chiral WSe_2 (CWS), serving as a structural origin of symmetry breaking, induces a pronounced spin-momentum locking effect due to asymmetric spin-orbit coupling (SOC) introduced by helical distortion. This effect subsequently stabilizes the *OCCO intermediate, which markedly lowers the activation energy barrier for C–C coupling. Spin-polarized density functional theory (DFT) calculations incorporating SOC reveal that the helical distortion breaks inversion symmetry and generates an asymmetric spin-dependent potential landscape, producing momentum-locked spin textures and valley-contrasting Berry curvature. These spin-geometric features enable carrier populations near the band edges and induce localized spin polarization at the catalytic interface. At the catalytic interface, this chiral environment enhances *OCCO adsorption through stronger orbital overlap and interfacial charge transfer. Concurrently, out-of-plane lattice distortion facilitates electronic delocalization and spin-matched hybridization between CWS surface and adsorbed state *OCCO, thereby efficiently driving the conversion of *OCCO to the final product. This study establishes a quantum design principle for chiral helical catalysts that harnesses chirality-induced spin polarization to enhance CO_2 conversion into multi-carbon products.

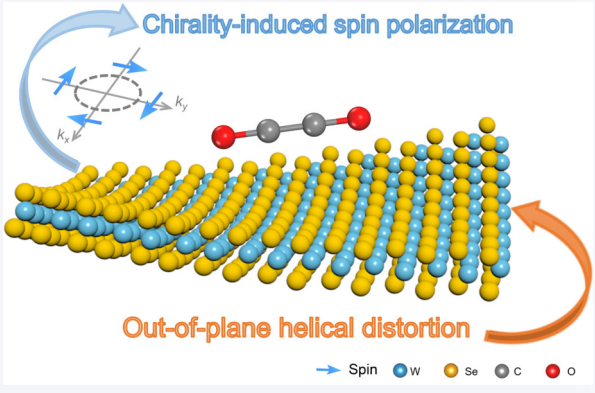

KEYWORDS: out-of-plane helical distortion, chirality-induced spin polarization, C–C coupling, density functional theory

1 Introduction

The electrochemical and photocatalytic conversion of CO_2 into value-added multi-carbon (C_{2+}) products provides a promising pathway for sustainable energy storage and carbon recycling [1–3]. However, the efficient formation of C–C bonds remains a major challenge because of the high energy barriers and spin constraints associated with stabilizing the *OCCO intermediate [4, 5]. Although copper-based catalysts can facilitate C–C coupling, their practical applications are restricted by limited C_{2+} selectivity, complex surface reconstructions, and high overpotentials at industrially relevant current densities [6–8]. Overcoming these limitations requires a fundamental reconfiguration of the catalytic environment that can simultaneously stabilize the *OCCO species and enable spin-allowed electron-transfer channels during the formation of the *OCCO intermediate.

Recent studies have highlighted that chiral structures, particularly those with helical distortions, can unlock unconventional catalytic mechanisms by creating a unique local environment for key reaction intermediates [9, 10]. In diverse chiral inorganic nanocatalysts, helical lattice distortion is a key driver for the efficient conversion of CO_2 to multi-carbon products [11–16]. These findings converge on a unifying design principle: The helical distortion inherent in chiral structures can serve as a critical geometric factor to reshape the catalytic interface, preferentially stabilizing key multi-carbon intermediates and steering reaction pathways toward products that are challenging to form on achiral surfaces.

Received: October 24, 2025; **Revised:** November 25, 2025
Accepted: December 20, 2025

✉Address correspondence to Yuxi Fang, sjtu15901600323@sjtu.edu.cn; Shunai Che, chesa@sjtu.edu.cn

Two-dimensional transition metal dichalcogenides, such as WSe_2, endowed with chirality would provide a tunable platform for realizing this concept. Their strong intrinsic spin-orbit coupling (SOC) and valley-contrasting Berry curvature make them especially responsive to symmetry-breaking modifications that rearrange spin and valley degrees of freedom [17–20]. In inversion-broken environments—whether from external fields, substrate interactions, or intentional lattice distortion—SOC, together with an asymmetric potential, can produce spin-momentum correlated electronic states and enhance Berry curvature near band edges [21–23]. This creates localized spin-polarized channels accessible under optical or electrochemical excitation. Introducing controlled helical distortions into a WSe_2 monolayer further amplifies these spin-geometric effects [24, 25]. The resulting chiral potential first induces momentum-dependent orbital angular momentum (L_z) polarization, SOC, then acts as a quantum bridge, converting this orbital polarization into a fixed spin texture aligned with the structural handedness.

In this work, we investigated chiral WSe_2 (CWS) as a catalyst for converting CO_2 into C_{2+} products. Using spin-polarized density functional theory (DFT) that includes explicit SOC, we constructed a series of enantiomorphic WSe_2 models with controlled out-of-plane torsion angles ranging from 3° to 11°. The central aspect of this study is a systematic comparison with centrosymmetric, achiral WSe_2 (AWS), which serves as an inert reference. We specifically examined how the introduction of structural chirality influences key electronic descriptors, such as electronic asymmetry, spin texture, and Berry curvature, relative to the AWS model. This comparative framework enables a direct correlation between these chiral electronic characteristics and the adsorption energetics of the *OCCO intermediate, thereby elucidating the structure–activity relationships that govern spin-polarized catalysis.

2 Methods

2.1 Computational framework

All DFT calculations were performed using the Vienna *ab initio* simulation package (VASP) with the projector augmented-wave (PAW) method [26–28]. The exchange-correlation energy was treated within the generalized gradient approximation (GGA) using the Perdew–Burke–Ernzerhof (PBE) functional [29, 30]. SOC was explicitly included in all electronic-structure calculations to capture relativistic effects essential for transition-metal dichalcogenides. The plane-wave kinetic energy cutoff was set to 500 eV, and the electronic self-consistent convergence threshold was 10^{-6} eV. Geometry optimizations were carried out until the Hellmann–Feynman forces on each atom were smaller than 0.01 eV·Å^{-1}. The Brillouin zone was sampled with a Monkhorst–Pack k-point grid of 4 × 5 × 1 for both structure relaxations and static calculations. Gaussian smearing with a width of 0.01 eV was applied for partial occupancies. A vacuum region of at least 20 Å was introduced along the z direction to prevent spurious interactions between periodic images.

2.2 Structural models of CWS

A rectangular 2 × 3 × 1 supercell of monolayer WSe_2 was constructed as the reference configuration, as shown in Fig. 1(a) and Fig. S1 in the Electronic Supplementary Material (ESM). The chirality of the CWS structure can be controlled by selecting different torsional axes. Specifically, using the two diagonals of a monolayer WSe_2 nanosheet as the torsional axes. A left-handed chiral WSe_2 (LWS) was formed when one diagonal is chosen as the fixed axis, and the two adjacent corners were twisted by a specific angle θ around this axis. Correspondingly, a right-handed chiral WSe_2 (RWS) was obtained by fixing the other diagonal and repeating the same twisting operation. The distortion angles were set to 3°, 5°, 7°, 9°, and 11° to examine chirality-dependent effects (Fig. S2 in the ESM). A vacuum spacing of 20 Å along the z-axis was maintained to eliminate interlayer interactions. All atomic positions were fully relaxed except for the constrained atoms defining the chiral distortion axis.

2.3 Berry curvature and spin analysis

The electronic geometric and spin-resolved properties were evaluated from first-principles calculations of the Berry curvature

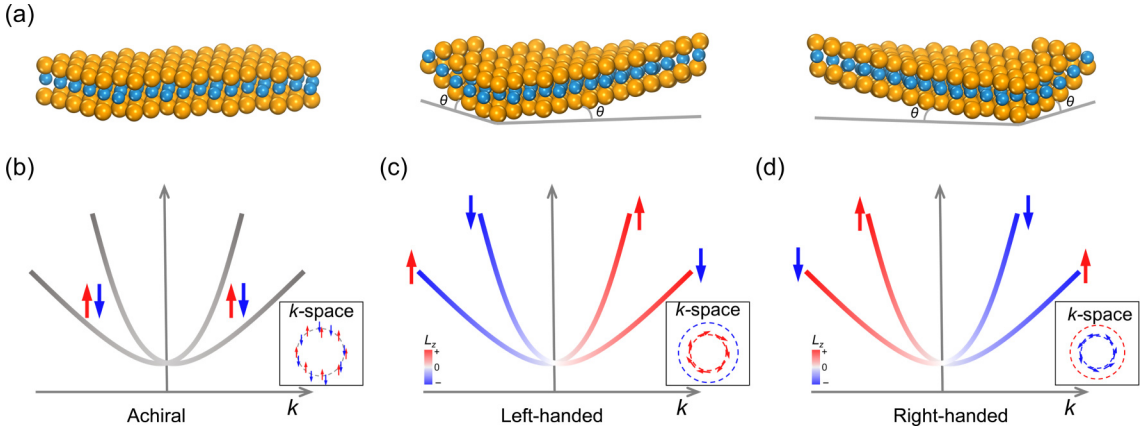

Figure 1 CWS design and chirality-induced spin polarization. (a) Out-of-plane θ-angle distortions introduced into AWS monolayers generate LWS and RWS nanostructures. The imposed structural chirality breaks inversion symmetry, establishing a chiral potential that couples spin and orbital degrees of freedom. (b) In the centrosymmetric AWS, the band structure remains spin-degenerate, with randomized spin orientations (red/blue arrows) in momentum space indicating the absence of spin-momentum locking. ((c) and (d)) In chiral systems ($\theta \neq 0°$), the chiral potential lifts the spin degeneracy via SOC. This process converts the orbital polarization into a momentum-dependent spin texture. (c) The left-handed configuration exhibits a clockwise spin vortex, consistent with its specific L_z polarization and the left-hand rule. (d) The right-handed counterpart shows a counterclockwise vortex, following the right-hand rule and mirroring the L_z profile. The vertical arrows along the bands denote spin orientations at specific momenta k, illustrating spin-momentum locking. These enantiomer-specific spin textures, which are mirror opposites while maintaining identical energy dispersions, directly manifest the chirality-induced spin polarization mediated by asymmetric SOC.

and spin texture. The band-resolved Berry curvature, $\Omega_n(k)$, where Ω is the Berry curvature, n is the band index, and k is the momentum, was computed for the z component in two-dimensional systems using the Kubo formula [31]. The Berry curvature $\Omega_n(k)$ was calculated in units of Å^2, with its sign following the right-hand convention for the reciprocal coordinate system (k_x, k_y, k_z)

$$\Omega_n^z(k) = -2\mathrm{Im}\sum_{m\neq n}\frac{\langle u_{nk}|\hat{v}_x|u_{mk}\rangle\langle u_{mk}|\hat{v}_y|u_{nk}\rangle}{(\varepsilon_{mk}-\varepsilon_{nk})^2} \quad (1)$$

where $|u_{mk}\rangle$ and $|u_{nk}\rangle$ represent the cell-periodic parts of the Bloch states for the m^{th} and n^{th} bands, respectively, $\hat{v}_x$ and $\hat{v}_y$ are the velocity operators, and ε_{nk} is the band energy. The calculations were performed on a uniform k grid using the VASPBERRY code [32, 33], which extracts Berry curvature values from the converged wavefunctions. Separate analyses were carried out for the valence-band maximum (VBM, n = 312) and the conduction-band minimum (CBM, n = 313) to assess spin-dependent transport channels of photoexcited carriers. Integrations over energy windows (bands 310–316) captured the collective contribution of photoactive states, while full occupied-band integrations (bands 1–312) were used to confirm a total Chern number near zero, consistent with the time-reversal symmetry of nonmagnetic systems.

The spin texture $S_n(k) = \langle\psi_{nk}|\boldsymbol{\sigma}|\psi_{nk}\rangle$ (where $|\psi_{nk}\rangle$ and $\langle\psi_{nk}|$ represent the spinor Bloch wavefunction and its complex conjugate for the n^{th} band at momentum k, respectively, and $\boldsymbol{\sigma}$ is the vector of Pauli spin matrices) comprising components S_x, S_y, and S_z was extracted from converged noncollinear SOC wavefunctions. Using the spin-texture module in VASP Post-Processing Toolkit (VASPKIT) [34], k-resolved spin expectation values were obtained from the wavefunction file (WAVECAR) and projected character file (PROCAR) outputs and interpolated onto a dense k-mesh. The in-plane spin components (S_x, S_y) were visualized as vector arrows, while the out-of-plane component (S_z) was represented by color mapping to illustrate the momentum-dependent spin orientation characteristic of chiral-induced spin selectivity (CISS). All results were verified to be converged with respect to both k-mesh density and the number of included bands.

2.4 Adsorption energy and reaction pathway calculations

The adsorption energies of CO_2 reduction intermediates, including *CO and *OCCO, were evaluated on both AWS and CWS surfaces. Adsorbates were placed on all symmetry-inequivalent sites, and the adsorption energy (E_{ads}) was calculated as [35]

$$E_{\text{ads}} = E_{\text{slab+adsorbate}} - E_{\text{slab}} - E_{\text{adsorbate}} \quad (2)$$

where $E_{\text{slab+adsorbate}}$ is the total energy of the combined system, E_{slab} is the energy of the clean slab, and $E_{\text{adsorbate}}$ is the energy of the isolated gas-phase molecule. All adsorption configurations were relaxed for different spin alignments until the forces converged within the defined threshold.

Reaction pathways were explored using the climbing image nudged elastic band (CI-NEB) method [36, 37] to obtain the minimum energy paths (MEPs) for key steps, such as *CO + *CO → *OCCO formation and subsequent hydrogenation. Each path consisted of three intermediate images, along with fixed initial and final states, to resolve the reaction coordinate. Elastic spring constants between images were set between 1 and 5 eV·Å^{-2}, and convergence was achieved when the maximum force on each image was below 0.03 eV·Å^{-1}. The climbing-image algorithm was used to accurately identify the transition state (TS), and the forces were refined to within 0.02 eV·Å^{-1}. Transition states were validated by vibrational frequency analysis using finite atomic displacements of 0.01–0.02 Å, confirming the presence of a single imaginary mode associated with the reaction coordinate.

Gibbs free energies at 298.15 K were obtained by including zero-point energy (ZPE) and thermal corrections derived from harmonic vibrational frequencies according to [38, 39]

$$G(T) = E_{\text{DFT}} + E_{\text{ZPE}} + \Delta H_{\text{vib}}(T) - TS(T) \quad (3)$$

where $G(T)$ is the Gibbs free energy at temperature T, E_{DFT} is the total electronic energy, E_{ZPE} is the zero-point energy, $\Delta H_{\text{vib}}(T)$ is the vibrational enthalpy, and $S(T)$ is the entropy. For adsorbed species, vibrational contributions were evaluated within the harmonic approximation for both the adsorbate and surface atoms, while gas-phase molecules included translational and rotational contributions derived from ideal-gas partition functions at 1 atm. All Gibbs free energies reported in this study include ZPE and thermal corrections at standard conditions.

3 Results and discussion

3.1 Chirality-induced spin polarization in CWS

The deliberate introduction of structural chirality into an otherwise centrosymmetric WSe_2 monolayer provides a quantum pathway to break spin degeneracy without the need for external magnetic fields. As shown in Fig. 1(a), applying out-of-plane distortions with a torsional angle θ generates LWS and RWS configurations from the AWS parent lattice. This symmetry breaking establishes a chiral potential that induces a pronounced momentum-dependent orbital angular momentum polarization, characterized by opposite signs at the $+k$ and $-k$ points. Through the strong intrinsic SOC of W and Se atoms, which serves as an essential bridge linking orbital and spin degrees of freedom, this orbital polarization is coherently converted into a momentum-locked spin texture, directly manifesting the CISS effect [40].

In the centrosymmetric AWS (θ = 0°, Fig. 1(b)), the electronic bands remain spin-degenerate. Spin orientations show no correlation with crystal momentum, and the absence of a chiral potential leads to randomized spin distributions in momentum space, consistent with a spin-unpolarized ground state [41]. When chiral distortion is introduced ($\theta \neq 0°$), the system develops a nonzero L_z texture that breaks local inversion symmetry. The SOC interaction, proportional to $L \cdot S$, lifts the spin degeneracy and maps the chiral orbital information onto a momentum-dependent spin alignment. This coupling effectively acts as a spin-polarized filter, transmitting one spin orientation preferentially along the transport direction [42].

In the LWS configuration (Fig. 1(c)), the spin texture in momentum space forms a clockwise vortex that follows the left-hand rule. This pattern originates from the intrinsic orbital polarization, where the chiral potential generates a specific L_z distribution that determines the spin orientation through strong SOC. The resulting spin-momentum alignment, in which positive L_z regions stabilize spin-down states while negative L_z regions favor spin-up configurations, demonstrates a deterministic L_z-to-spin mapping. Conversely, the RWS configuration (Fig. 1(d)) exhibits a

counterclockwise spin vortex that mirrors both the reversed L_z profile and the corresponding spin-momentum locking behavior. Both enantiomers retain identical energy dispersions, confirming that structural chirality is encoded in the helical organization of the spin texture, rather than in its band energy distribution. Although the spin texture exhibits a helical configuration, the total Chern number of the system remains zero, indicating a geometrically helical but topologically trivial spin configuration. The resulting spin-momentum correlation, where each handedness yields a unique and fixed relationship between electron momentum and spin orientation, underpins the CISS-driven spin filtering behavior, with the chiral orbital texture serving as the fundamental origin of spin polarization.

This enantiomer-specific spin texture introduces an additional quantum degree of freedom for controlling electronic and catalytic processes. Within the CISS framework, CWS behaves as a momentum-sensitive spin filter that stabilizes electronic states with specific spin alignment. Such spin-polarized channels can preferentially stabilize reaction intermediates, for instance, an adsorbed state *OCCO species during C–C coupling, by enabling spin-aligned charge transfer. The synergistic interplay of chiral symmetry breaking, L_z polarization, and SOC is calculated to reduce the activation barrier for *OCCO formation, establishing a direct connection between structural chirality, momentum space spin texture, and CISS-mediated catalytic reactivity in two-dimensional systems [43, 44].

3.2 Chirality-induced electronic structure evolution and emergent Berry curvature topology

The evolution of the spin-resolved band structures of LWS and RWS reveals that mirrored structural handedness reverses the helicity of the momentum-dependent spin texture while preserving the overall energy dispersion. Figure 2 shows the results for LWS, and the corresponding data for RWS are provided in Fig. S3 in the ESM. In the centrosymmetric AWS, the bands remain spin-degenerate across the Brillouin zone (Fig. 2(a)), consistent with preserved inversion symmetry and the absence of net spin polarization. Introducing a small torsional distortion (θ = 3°) to form LWS lifts this degeneracy immediately (Fig. 2(b)). Distinct energy splitting appears near high-symmetry points, and the resulting subbands exhibit complementary spin characteristics: one dominated by spin-up (red) and the other by spin-down (blue), forming a well-defined momentum-correlated spin texture. Within the framework of CISS, this phenomenon originates from the chiral potential created by structural distortion. The breaking of inversion symmetry, combined with the intrinsic SOC of W and Se atoms, converts geometric handedness into a momentum-dependent spin-polarized filter that couples carrier momentum to spin orientation, producing enantiomer-specific spin textures in the electronic structure [45, 46].

As the torsion angle increases from 3° to 11°, the spin-polarized energy gap evolves systematically (Figs. 2(c)–2(f)). This angular dependence highlights the direct correlation between the degree of structural chirality and the magnitude of spin polarization. Greater torsional distortion enhances the chiral potential, which in turn amplifies SOC-mediated band separation. The calculated band structures also reveal clear signatures of spin-momentum correlation: The energy of a spin-polarized state varies periodically along specific momentum directions, giving rise to a characteristic spin texture. A direct comparison between LWS (Fig. 2) and RWS (Fig. S3 in the ESM) confirms that the two enantiomers exhibit opposite spin polarization directions at equivalent k-points for the same band branch. For instance, at the K point, the same branch is spin-up (red) polarized in LWS but spin-down (blue) polarized in RWS. This enantiomer-specific spin reversal represents the microscopic origin of the CISS effect and indicates that chiral WSe_2 supports highly spin-polarized charge transport.

To further explore the topological electronic properties arising from structural chirality, we analyzed the Berry curvature distribution and momentum space spin texture (Fig. 3 and Figs. S4–S8 in the ESM). The Berry curvature captures the geometric phase of the Bloch states, while the spin texture directly visualizes the microscopic manifestation of spin-momentum coupling [47, 48]. In AWS (Fig. 3(a)), the Berry curvature is nearly uniform and close to zero throughout the Brillouin zone, consistent with a topologically trivial state maintained by time-reversal symmetry. Introducing structural chirality produces strong local variations, with pronounced positive (red) and negative (blue) Berry curvature peaks localized near the corners of the hexagonal Brillouin zone

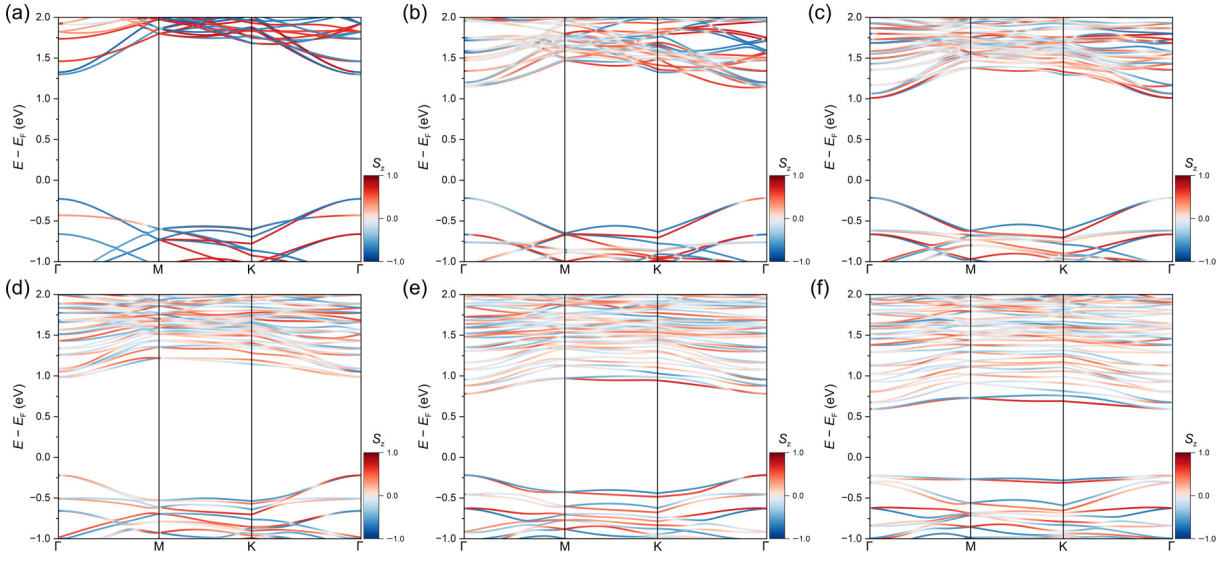

Figure 2 Evolution of spin-resolved band structures with increasing distortion angle. Band structures of (a) the achiral AWS and ((b)–(f)) the LWS at torsional angles of 3°–11°. The S_z is color-coded: red ($S_z > 0$) denotes spin-up and blue ($S_z < 0$) denotes spin-down.

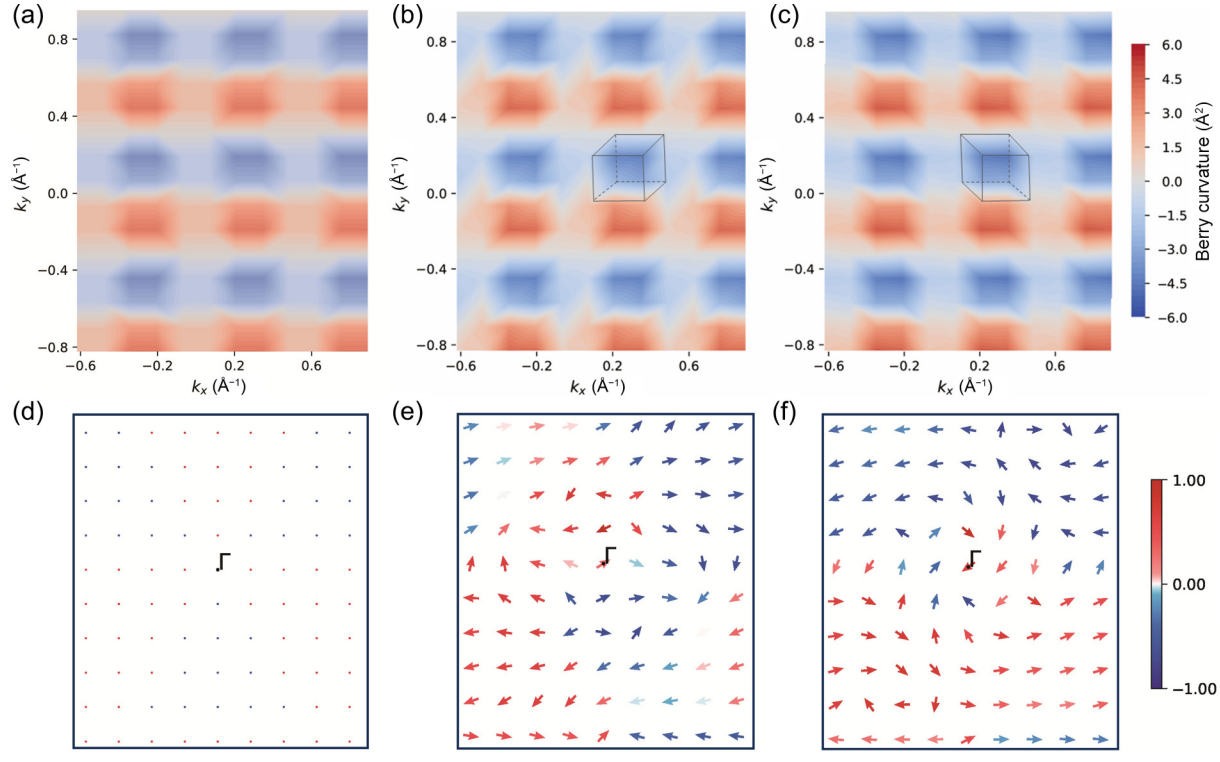

Figure 3 Chirality-induced Berry curvature and spin texture. ((a)–(c)) Berry curvature distribution for all occupied electronic bands in (a) AWS, (b) LWS, and (c) RWS. Red and blue colors correspond to positive and negative curvature values. The first Brillouin zone is outlined in white, with an overlaid cubic unit-cell schematic indicating high-symmetry directions. ((d)–(f)) Momentum space spin texture at the valence-band maximum for (d) AWS, (e) LWS, and (f) RWS. The arrow direction represents the in-plane spin polarization direction, while the color indicates the magnitude of the S_z.

valleys (Figs. 3(b) and 3(c)). These features confirm that the breaking of inversion symmetry by chiral distortion generates nonzero local Berry curvature. Moreover, the Berry curvature distributions of LWS and RWS display approximate mirror symmetry, being opposite in sign at corresponding k-points and satisfying the relation $\Omega_{\mathrm{LWS}}(k) = -\Omega_{\mathrm{RWS}}(-k)$ under spatial inversion.

The spin texture near the valence-band maximum further supports these observations. In AWS, the spin orientations appear disordered, showing negligible in-plane alignment and weak S_z, consistent with spin degeneracy (Fig. 3(d)). In contrast, both LWS and RWS develop well-defined vortex-like spin textures. These vortices exhibit clear spin-momentum correlation: The in-plane spins form closed loops perpendicular to the momentum direction, while the S_z follows a handedness-dependent pattern. Notably, LWS and RWS display opposite vortex helicities and reversed S_z signs in corresponding valleys, providing direct evidence of enantiomer-specific spin polarization (Figs. 3(e) and 3(f)). Overall, the Berry curvature and spin texture analyses demonstrate that structural chirality not only induces spin polarization but also modifies the topological features of the electronic structure. The emergence of finite Berry curvature implies that chirality can generate transverse charge transport under an applied electric field [49, 50].

3.3 Chirality-induced enhancement in *OCCO adsorption energy and C–C coupling

Figure 4 presents the adsorption energetics, atomic configurations, and electronic structure of the *OCCO intermediate on AWS and CWS, demonstrating how out-of-plane structural chirality governs surface reactivity. Quantitatively, both LWS and RWS exhibit stronger OCCO binding than AWS, even though OCCO itself is achiral (Fig. 4(a)). The equivalent adsorption energies of LWS and RWS indicate that the enhancement originates not from molecular handedness but from inversion symmetry breaking within the substrate that modifies its local electronic potential. The nearly identical enhancement of both enantiomers confirms that the stronger binding is a direct consequence of symmetry breaking rather than enantiospecific interaction. Similar parity in enantiomeric adsorption has been observed in chiral but nonmagnetic systems where structural chirality affects charge redistribution and orbital hybridization symmetrically [51–53]. The optimized adsorption geometries (Fig. 4(b)) provide a direct structural explanation for this enhanced binding. The chiral distortion causes local bending of the W–Se lattice, producing tilted adsorption geometries in which the O and C atoms of *OCCO approach surface W atoms more closely than in AWS. This geometric realignment, together with the built-in out-of-plane electric field ($E_\perp$) arising from chirality, enhances the local electrostatic potential gradient, thereby amplifying interfacial orbital coupling and electron sharing between the surface and the adsorbate [54].

The projected density of states (PDOS) offers a clear electronic signature of these effects. In AWS, the W-5d orbitals dominate near the Fermi level, while the C-2p and O-2p contributions are weak, indicating limited hybridization. In contrast, both 5°-LWS and 11°-LWS display broadened hybrid bands extending from −4 to +2 eV, accompanied by reduced W-d intensity, signifying stronger orbital mixing and enhanced electron delocalization. The 11°-LWS case is particularly revealing, showing a hybridized state partially crossing the Fermi level, which implies charge transfer from W-5d to

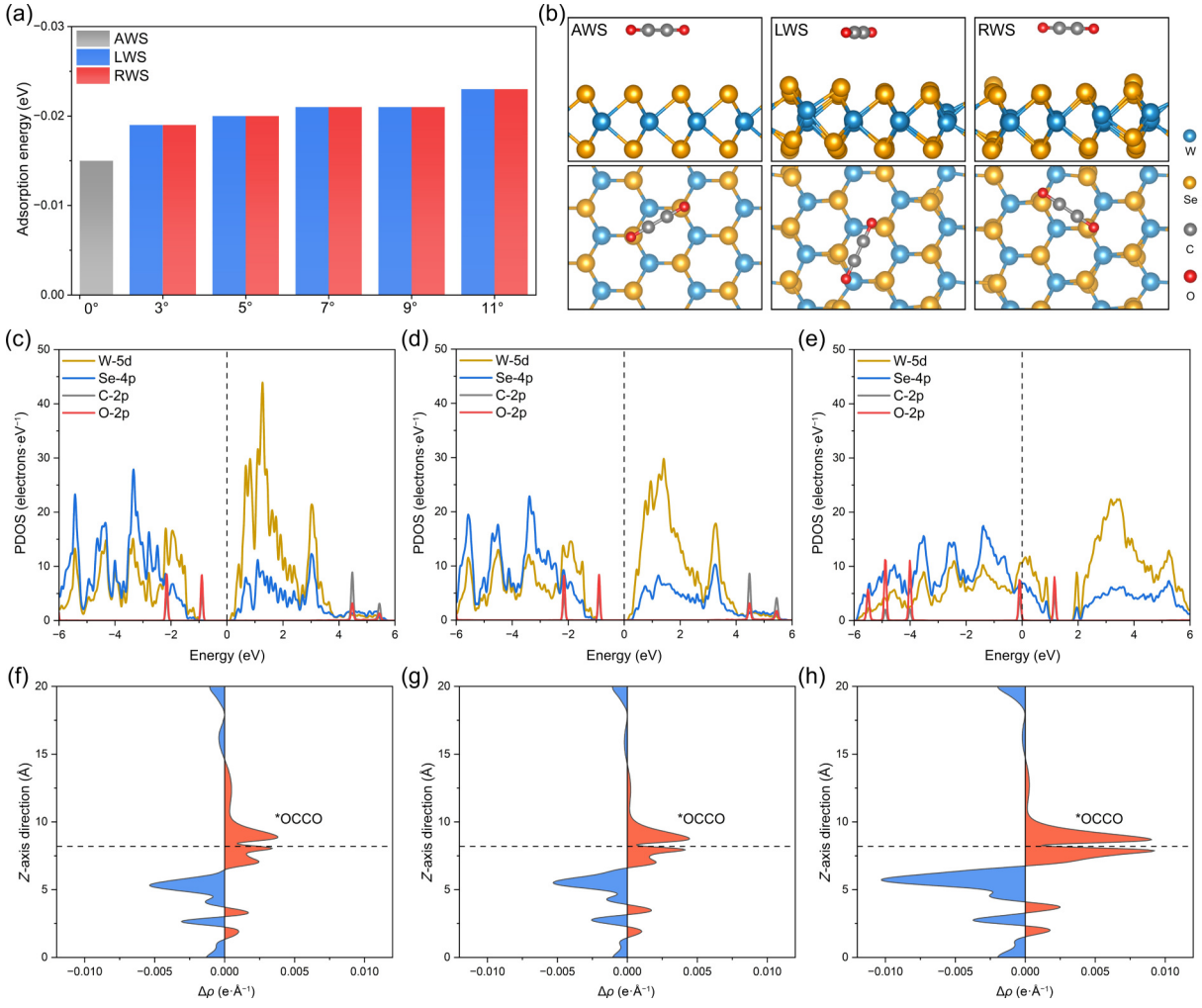

Figure 4 *OCCO intermediate adsorption on CWS. (a) Adsorption energies of *OCCO on AWS, and CWS with torsion angle (θ = 3°–11°). (b) Optimized adsorption geometries for AWS, 11°-LWS, and 11°-RWS (side and top views). Chiral distortion tilts *OCCO closer to the surface and enhances orbital overlap. ((c)–(e)) PDOS for AWS, 5°-LWS, and 11°-LWS after *OCCO adsorption. ((f)–(h)) Plane-averaged charge-density differences ($\Delta\rho$) for AWS, 5°-LWS, and 11°-LWS. Red and blue regions denote electron accumulation and depletion.

*OCCO antibonding orbitals (Figs. 4(d) and 4(e) and Fig. S9 in the ESM). This near-Fermi hybridization produces a metallic-like interface that promotes electronic communication between the substrate and adsorbate. A comparable correlation between structural chirality, SOC-driven orbital delocalization, and enhanced interfacial conductivity has been reported in chiral topological semiconductors [55].

The plane-averaged charge-density differences (Figs. 4(f)–4(h)) directly visualize these charge rearrangements. Compared to AWS, both 5°-LWS and 11°-LWS exhibit pronounced charge accumulation near OCCO and depletion around neighboring Se atoms, confirming stronger electronic coupling at the interface. This monotonic growth demonstrates that increasing torsion strengthens electron delocalization across the interface, in agreement with the PDOS results. The out-of-plane chirality thus acts as a structural driver for electron redistribution, generating an asymmetric potential gradient that facilitates directional charge flow. Collectively, out-of-plane distortion in CWS amplifies OCCO adsorption through three cooperative effects: enhanced orbital overlap, increased charge transfer, and orbital hybridization. The nearly identical adsorption energies of LWS and RWS verify that these effects arise from inversion symmetry breaking rather than molecular handedness. The resulting orbital hybridization interface establishes a more favorable energetic pathway for C–C coupling and provides a unified microscopic framework for understanding chirality-driven catalytic enhancement in CWS.

To evaluate how adsorption influences reaction kinetics, we calculated the free-energy profiles for the C–C coupling step in CO_2 reduction (Fig. 5(a)) and analyzed the corresponding transition-state geometries (Figs. 5(b)–5(d)). The computed energy landscapes reveal a clear dependence on the degree of out-of-plane chiral distortion. As depicted in Fig. 5(a), the AWS surface exhibits the largest activation barrier, indicating sluggish C–C coupling kinetics. In contrast, the introduction of chiral distortion reduces the barrier significantly, with 5°-LWS and 11°-LWS showing progressively lower activation energies as the torsion angle increases. This reduction correlates with increasing chiral distortion angle, consistent with the enhanced orbital hybridization and electronic asymmetry observed in the band structure and Berry curvature analyses (Figs. 2 and 3). The correlation directly links catalytic improvement to the out-of-plane lattice distortion, which alters the surface electronic structure and enhances orbital asymmetry at the reaction interface. Meanwhile, we discuss the free energy of the competing hydrogen evolution reaction (HER) in Fig. S12 in the

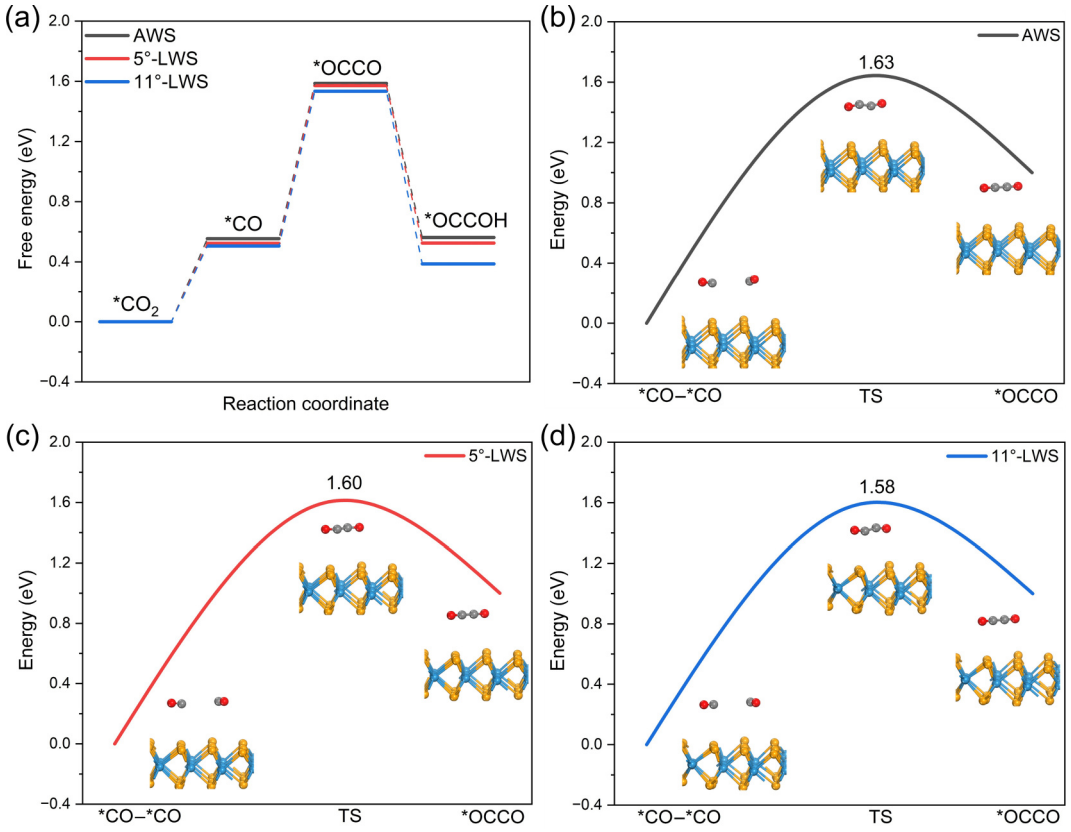

Figure 5 Chirality-enhanced catalytic mechanism for C–C coupling. (a) Free energy profiles for the C–C coupling reaction on AWS, 5°-LWS, and 11°-LWS. ((b)–(d)) Calculated energy barriers of the transition states for AWS, 5°-LWS, and 11°-LWS. The lower energy barrier observed in chiral catalysts demonstrates that structural chirality facilitates C–C coupling by stabilizing key intermediates and transition states.

ESM. The results show that the HER barrier on the 11°-LWS surface is substantially higher than that on the AWS, indicating an inherent suppression of the HER on the chiral catalysts. This suppression of the competing HER reveals a dual beneficial effect of the chiral design strategy.

At the microscopic level, the out-of-plane chirality introduces an asymmetric electrostatic potential gradient perpendicular to the basal plane. This structural asymmetry perturbs the distribution of the W-5d orbitals and redistributes their angular momentum components, leading to anisotropic orbital interactions. The resulting orbital realignment strengthens electronic coupling between adsorbed *CO species and the CWS surface, facilitating charge transfer and stabilizing the transition state [56, 57]. During the *CO + *CO → *OCCO step, the geometrically induced orbital overlap enables more efficient bond formation and effectively lowers the reaction barrier for C–C coupling. The combined effects of out-of-plane helical distortion-induced orbital realignment, enhanced electronic delocalization, and facilitated charge transfer collectively constitute the microscopic mechanism by which the structural chirality lowers the reaction barrier observed in Fig. 5(a).

Structural examination of the transition states supports this mechanism. On AWS, the two *CO species remain spatially separated with limited orbital overlap, producing an elongated and energetically unfavorable configuration. In contrast, chiral LWS catalysts display pre-organized transition states where the two *CO adopt nearly coplanar geometries with shortened C···C distances, closely approximating the final *OCCO product. This geometric convergence arises from the out-of-plane helical distortion, which enhances orbital overlap between the adsorbates and the W–Se surface states, reduces electronic repulsion, and promotes the formation of C–C bonds. Consequently, the out-of-plane chiral distortion functions as a structural template that optimizes the spatial alignment and orbital overlap of the reacting *CO species, guiding them toward a more favorable transition-state geometry and generating a lower-energy reaction pathway that facilitates C–C coupling.

Collectively, these findings demonstrate that out-of-plane helical distortion in CWS serves as a quantum geometric lever that regulates surface orbital interactions, strengthens electronic coupling between adsorbates and the catalyst surface, and stabilizes the C–C coupling transition state. This geometric modulation provides a unified microscopic explanation for the chirality-dependent reduction of reaction barriers, establishing a direct link between structural handedness, orbital reorganization, and enhanced catalytic kinetics.

4 Conclusions

In summary, this study reveals a quantum pathway by which geometric chirality in monolayer WSe_2 couples to spin-dependent electronic responses and thereby enhances catalytic conversion of CO_2 into multi-carbon products. Specifically, an out-of-plane helical distortion activates SOC and generates valley-polarized Berry curvature. Spin-polarized DFT calculations that include explicit SOC show that this out-of-plane helical distortion breaks inversion symmetry and produces momentum-dependent spin-polarized states with opposite helicities in the two enantiomeric forms. As a result, the system exhibits spin-momentum locking and valley-

contrasting Berry curvature hotspots. Mechanistically, the out-of-plane helical distortion reshapes the local electronic environment and modifies orbital overlap at the adsorption site, which drives charge redistribution and stabilizes the *OCCO intermediate. This stabilization lowers the activation barrier for C–C coupling by optimizing orbital alignment and facilitating charge delocalization during bond formation. Projected density of states and charge-density difference analyses further confirm enhanced orbital hybridization and asymmetric charge redistribution induced by the out-of-plane helical distortion. Collectively, these results establish a direct quantum connection between geometric chirality and catalytic reactivity and define a design paradigm for two-dimensional chiral catalysts in which out-of-plane structural modulation acts as a structural degree of freedom that modulates SOC and charge redistribution to promote efficient CO_2 conversion into multi-carbon products. Future work should prioritize the synthesis and engineering of chiral materials with tailored out-of-plane spin textures to further improve catalytic performance.

Electronic Supplementary Material: Supplementary material (atomic structure; spin-resolved band structures of RWS; Berry curvature distribution for all occupied bands, energy-window-resolved bands, VBM and CBM; element-resolved magnetic moment PDOS; CO_2 adsorption behavior; charge-density difference maps; and thermodynamic quantities for CO_2 reduction) is available in the online version of this article at https://doi.org/10.26599/NR.2026.94908369.

Data availability

All data needed to support the conclusions in the paper are presented in the manuscript and the Electronic Supplementary Material. Additional data related to this paper may be requested from the corresponding author upon request.

Acknowledgements

We would like to thank Professor Chungang Duan from East China Normal University for his insightful discussions and valuable suggestions on this work. This work was supported by the National Key R&D Program of China (No. 2021YFA1200301), the National Natural Science Foundation of China (No. 22501180), Shanghai Natural Science Foundation (No. 25ZR1402587), Shanghai Titan Natural Science Development Foundation (No. FF0010561), and Shanghai Pilot Program for Basic Research-Shanghai Jiao Tong University (No. 21TQ1400219).

Declaration of competing interest

All the contributing authors report no conflict of interests in this work.

Author contribution statement

T. W. O.: Data curation, data analysis, computational design, writing manuscript. H. S.: Data analysis. S. A. C.: Project administration, funding acquisition, validation, review & editing. Y. X. F.: Project administration, funding acquisition, validation, computational design, review & editing. All the authors have approved the final manuscript.

Use of AI statement

None.

References

[1] Rao, H.; Schmidt, L. C.; Bonin, J.; Robert, M. Visible-light-driven methane formation from CO_2 with a molecular iron catalyst. *Nature* **2017**, *548*, 74–77.

[2] Huang, J. E.; Li, F. W.; Ozden, A.; Sedighian Rasouli, A.; García de Arquer, F. P.; Liu, S. J.; Zhang, S. Z.; Luo, M. C.; Wang, X.; Lum, Y. et al. CO_2 electrolysis to multicarbon products in strong acid. *Science* **2021**, *372*, 1074–1078.

[3] Zhou, B. W.; Ma, Y. J., Ou, P. F.; Ye, Z. W.; Li, X. Y.; Vanka, S.; Ma, T.; Sun, H. D.; Wang, P.; Zhou, P. et al. Light-driven synthesis of C_2H_6 from CO_2 and H_2O on a bimetallic AuIr composite supported on InGaN nanowires. *Nat. Catal.* **2023**, *6*, 987–995.

[4] Ma, Z. S.; Yang, Z. L.; Lai, W. C.; Wang, Q. Y.; Qiao, Y.; Tao, H. L.; Lian, C.; Liu, M.; Ma, C.; Pan, A. L. et al. CO_2 electroreduction to multicarbon products in strongly acidic electrolyte via synergistically modulating the local microenvironment. *Nat. Commun.* **2022**, *13*, 7596.

[5] Mato, J.; Poole, D.; Gordon, M. S. Stability and dissociation of ethylenedione (OCCO). *J. Phys. Chem. A* **2020**, *124*, 8209–8222.

[6] Kortlever, R.; Peters, I.; Balemans, C.; Kas, R.; Kwon, Y.; Mul, G.; Koper, M. T. M. Palladium-gold catalyst for the electrochemical reduction of CO_2 to C_1–C_5 hydrocarbons. *Chem. Commun.* **2016**, *52*, 10229–10232.

[7] Yin, J.; Yin, Z. Y.; Jin, J.; Sun, M. Z.; Huang, B. L.; Lin, H. H.; Ma, Z. H.; Muzzio, M.; Shen, M. Q.; Yu, C. et al. A new hexagonal cobalt nanosheet catalyst for selective CO_2 conversion to ethanal. *J. Am. Chem. Soc.* **2021**, *143*, 15335–15343.

[8] Zhou, Y. S.; Martín, A. J.; Dattila, F.; Xi, S. B.; López, N.; Pérez-Ramírez, J.; Yeo, B. S. Long-chain hydrocarbons by CO_2 electroreduction using polarized nickel catalysts. *Nat. Catal.* **2022**, *5*, 545–554.

[9] Yang, S. H.; Naaman, R.; Paltiel, Y.; Parkin, S. S. P. Chiral spintronics. *Nat. Rev. Phys.* **2021**, *3*, 328–343.

[10] Naaman, R.; Paltiel, Y.; Waldeck, D. H. Chiral molecules and the electron spin. *Nat. Rev. Chem.* **2019**, *3*, 250–260.

[11] Zhang, W. N.; Ai, J.; Ouyang, T. W.; Yu, L.; Liu, A. K.; Han, L.; Duan, Y. Y.; Tian, C. L.; Chu, C. Y.; Ma, Y. H. et al. Chiral nanostructured Ag films for multicarbon products from CO_2 electroreduction. *J. Am. Chem. Soc.* **2024**, *146*, 28214–28221.

[12] Cui, Y. P.; Ai, J.; Duan, Y. Y.; Jia, M. H.; Ouyang, T. W.; Liu, A. K.; Yu, L.; Liu, J. H.; Liu, X.; Chu, C. Y. et al. Enantioselective synthesis of amino acids by photocatalytic reduction of CO_2 on chiral mesostructured ZnS. *Chem* **2025**, *11*, 102390.

[13] Cui, Y. P.; Wang, Y.; Ma, Y. H.; Su, X. Z.; Tai, R. Z.; Jia, M. H.; Chen, J. Q.; Liu, A. K.; Yu, L.; Tian, C. L. et al. A chiral mesostructured photocatalyst for efficient solar-driven CO_2 reduction to ethanol. *Nat. Synth.*, in press, DOI: 10.1038/s44160-025-00908-2.

[14] Liu, B.; Zhang, W. N.; Fang, Y. X.; Che, S. N. Enantiomeric discrimination by UV–Vis-absorption chiral anisotropy of chiral nanostructured Au particles. *Nano Res.* **2025**, *18*, 94907352.

[15] Chen, H.; Deng, Q. Z.; Ouyang, T. W.; Zhang, W. N.; Liu, B.; Han, L.; Che, S. N.; Fang, Y. X. Chiral nanostructured Pd films for efficient electrocatalytic reduction of nitrite to ammonia. *Chem. Eng. J.* **2025**, *512*, 162647.

[16] Zhang, W. N.; Wang, J.; Ouyang, T. W.; Han, L.; Duan, Y. Y.; Che, S. N.; Fang, Y. X. Efficient CO_2 electroreduction to CO on chiral nanostructured Au films. *ACS Catal.* **2025**, *15*, 12377–12385.

[17] Wang, Y.; Sarkar, S.; Yan, H.; Chhowalla, M. Critical challenges in the development of electronics based on two-dimensional transition metal dichalcogenides. *Nat. Electron.* **2024**, *7*, 638–645.

[18] Gupta, S.; Zhang, J. J.; Lei, J. C.; Yu, H.; Liu, M. J.; Zou, X. L.; Yakobson, B. I. Two-dimensional transition metal dichalcogenides: A theory and simulation perspective. *Chem. Rev.* **2025**, *125*, 786–834.

[19] Pack, J.; Guo, Y. J.; Liu, Z. Y.; Jessen, B. S.; Holtzman, L.; Liu, S.;

Cothrine, M.; Watanabe, K.; Taniguchi, T.; Mandrus, D. G. et al. Charge-transfer contacts for the measurement of correlated states in high-mobility WSe_2. *Nat. Nanotechnol.* **2024**, *19*, 948–954.
[20] Xie, J. X.; Zhang, Z. C.; Zhang, H. D.; Nagarajan, V.; Zhao, W. Y.; Kim, H. L.; Sanborn, C.; Qi, R. S.; Chen, S. D.; Kahn, S. et al. Low resistance contact to P-type monolayer WSe_2. *Nano Lett.* **2024**, *24*, 5937–5943.
[21] Chen, J. J.; Wu, K.; Hu, W.; Yang, J. L. Spin-orbit coupling in 2D semiconductors: A theoretical perspective. *J. Phys. Chem. Lett.* **2021**, *12*, 12256–12268.
[22] Dey, P.; Yang, L. Y.; Robert, C.; Wang, G.; Urbaszek, B.; Marie, X.; Crooker, S. A. Gate-controlled spin-valley locking of resident carriers in WSe_2 monolayers. *Phys. Rev. Lett.* **2017**, *119*, 137401.
[23] Robert, C.; Park, S.; Cadiz, F.; Lombez, L.; Ren, L.; Tornatzky, H.; Rowe, A.; Paget, D.; Sirotti, F.; Yang, M. et al. Spin/valley pumping of resident electrons in WSe_2 and WS_2 monolayers. *Nat. Commun.* **2021**, *12*, 5455.
[24] Ghorai, K.; Das, S.; Varshney, H.; Agarwal, A. Planar hall effect in quasi-two-dimensional materials. *Phys. Rev. Lett.* **2025**, *134*, 026301.
[25] Duan, S. Y.; Qin, F.; Chen, P.; Yang, X. P.; Qiu, C. Y.; Huang, J. W.; Liu, G.; Li, Z. Y.; Bi, X. Y.; Meng, F. H. et al. Berry curvature dipole generation and helicity-to-spin conversion at symmetry-mismatched heterointerfaces. *Nat. Nanotechnol.* **2023**, *18*, 867–874.
[26] Kohn, W.; Becke, A. D.; Parr, R. G. Density functional theory of electronic structure. *J. Phys. Chem.* **1996**, *100*, 12974–12980.
[27] Kresse, G.; Furthmüller, J. Efficiency of *ab initio* total energy calculations for metals and semiconductors using a plane-wave basis set. *Comput. Mater. Sci.* **1996**, *6*, 15–50.
[28] Kresse, G.; Furthmüller, J. Efficient iterative schemes for *ab initio* total-energy calculations using a plane-wave basis set. *Phys. Rev. B* **1996**, *54*, 11169–11186.
[29] Perdew, J. P.; Burke, K.; Ernzerhof, M. Generalized gradient approximation made simple. *Phys. Rev. Lett.* **1997**, *78*, 1396.
[30] Staroverov, V. N.; Scuseria, G. E.; Perdew, J. P.; Davidson, E. R.; Katriel, J. High-density limit of the Perdew–Burke–Ernzerhof generalized gradient approximation and related density functionals. *Phys. Rev. A* **2006**, *74*, 044501.
[31] Fu, B.; Shen, S. Q. $Z/2$ topological invariants and the half quantized Hall effect. *Commun. Phys*. **2025**, *8*, 2.
[32] Kim, S. W.; Kim, H. J.; Cheon, S.; Kim, T. H. Circular dichroism of emergent chiral stacking orders in quasi-one-dimensional charge density waves. *Phys. Rev. Lett.* **2022**, *128*, 046401.
[33] Fukui, T.; Hatsugai, Y.; Suzuki, H. Chern numbers in discretized Brillouin zone: Efficient method of computing (spin) hall conductances. *J. Phys. Soc. Japan* **2005**, *74*, 1674–1677.
[34] Wang, V.; Xu, N.; Liu, J. C.; Tang, G.; Geng, W. T. VASPKIT: A user-friendly interface facilitating high-throughput computing and analysis using VASP code. *Comput. Phys. Commun.* **2021**, *267*, 108033.
[35] Saini, S.; Halldin Stenlid, J.; Abild-Pedersen, F. Electronic structure factors and the importance of adsorbate effects in chemisorption on surface alloys. *npj Comput. Mater.* **2022**, *8*, 163.
[36] Zarkevich, N. A.; Johnson, D. D. Nudged-elastic band method with two climbing images: Finding transition states in complex energy landscapes. *J. Chem. Phys.* **2015**, *142*, 024106.
[37] Henkelman, G.; Uberuaga, B. P.; Jónsson, H. A climbing image nudged elastic band method for finding saddle points and minimum energy paths. *J. Chem. Phys.* **2000**, *113*, 9901–9904.
[38] Elm, J.; Bilde, M.; Mikkelsen, K. V. Assessment of density functional theory in predicting structures and free energies of reaction of atmospheric prenucleation clusters. *J. Chem. Theory Comput.* **2012**, *8*, 2071–2077.
[39] Ouyang, T. W.; Guo, J. Q.; Shen, H. C.; Mu, M. M.; Shen, Y. L.; Yin, X. H. The Z-scheme transfer of photogenerated electrons for CO_2 photocatalytic reduction over g-ZnO/2H-MoS_2 heterostructure. *Nanoscale* **2021**, *13*, 18192–18200.
[40] Ouyang, T. W.; Su, H.; Zhang, W. N.; Duan, Y. Y.; Fang, Y. X.; Che, S. N.; Liu, Y. Z. Photomagnetic-chiral anisotropy mediated by chirality-driven asymmetric spin splitting. *Phys. Rev. Lett.* **2025**, *135*, 166903.
[41] Kane, C. L.; Mele, E. J. Quantum spin hall effect in graphene. *Phys. Rev. Lett.* **2005**, *95*, 226801.
[42] Wan, L.; Liu, Y. Z.; Fuchter, M. J.; Yan, B. H. Anomalous circularly polarized light emission in organic light-emitting diodes caused by orbital-momentum locking. *Nat. Photonics* **2023**, *17*, 193–199.
[43] Adhikari, Y.; Liu, T. H.; Wang, H. L.; Hua, Z. Q.; Liu, H. Y.; Lochner, E.; Schlottmann, P.; Yan, B. H.; Zhao, J. H.; Xiong, P. Interplay of structural chirality, electron spin and topological orbital in chiral molecular spin valves. *Nat. Commun.* **2023**, *14*, 5163.
[44] Ai, M. H.; Pan, L.; Shi, C. X.; Huang, Z. F.; Zhang, X. W.; Mi, W. B.; Zou, J. J. Spin selection in atomic-level chiral metal oxide for photocatalysis. *Nat. Commun.* **2023**, *14*, 4562.
[45] Zollner, K.; Kurpas, M.; Gmitra, M.; Fabian, J. First-principles determination of spin-orbit coupling parameters in two-dimensional materials. *Nat. Rev. Phys.* **2025**, *7*, 255–269.
[46] Liu, Y. Z., Xiao, J. W., Koo, J.; Yan, B. H. Chirality-driven topological electronic structure of DNA-like materials. *Nat. Mater.* **2021**, *20*, 638–644.
[47] Xiao, D.; Chang, M. C.; Niu, Q. Berry phase effects on electronic properties. *Rev. Mod. Phys.* **2010**, *82*, 1959–2007.
[48] Krieger, J. A.; Stolz, S.; Robredo, I.; Manna, K.; McFarlane, E. C.; Date, M.; Pal, B.; Yang, J. B.; Guedes, E. B.; Dil, J. H. et al. Weyl spin-momentum locking in a chiral topological semimetal. *Nat. Commun.* **2024**, *15*, 3720.
[49] Sinova, J.; Valenzuela, S. O.; Wunderlich, J.; Back, C. H.; Jungwirth, T. Spin Hall effects. *Rev. Mod. Phys.* **2015**, *87*, 1213–1260.
[50] Calavalle, F.; Suárez-Rodríguez, M.; Martín-García, B.; Johansson, A.; Vaz, D. C.; Yang, H. Z.; Maznichenko, I. V.; Ostanin, S.; Mateo-Alonso, A.; Chuvilin, A. et al. Gate-tuneable and chirality-dependent charge-to-spin conversion in tellurium nanowires. *Nat. Mater.* **2022**, *21*, 526–532.
[51] Lee, H.; Lee, C. U.; Yun, J.; Jeong, C. S.; Jeong, W.; Son, J.; Park, Y. S.; Moon, S.; Lee, S.; Kim, J. H. et al. A dual spin-controlled chiral two-/three-dimensional perovskite artificial leaf for efficient overall photoelectrochemical water splitting. *Nat. Commun.* **2024**, *15*, 4672.
[52] Nakajima, R.; Hirobe, D.; Kawaguchi, G.; Nabei, Y.; Sato, T.; Narushima, T.; Okamoto, H.; Yamamoto, H. M. Giant spin polarization and a pair of antiparallel spins in a chiral superconductor. *Nature* **2023**, *613*, 479–484.
[53] Naaman, R.; Paltiel, Y.; Waldeck, D. H. Chiral induced spin selectivity and its implications for biological functions. *Annu. Rev. Biophys.* **2022**, *51*, 99–114.
[54] Xiao, D.; Liu, G. B.; Feng, W. X.; Xu. X. D.; Yao, W. Coupled spin and valley physics in monolayers of MoS_2 and other group-VI dichalcogenides. *Phys. Rev. Lett.* **2012**, *108*, 196802.
[55] Yen, Y.; Krieger, J. A.; Yao, M. Y.; Robredo, I.; Manna, K.; Yang, Q.; McFarlane, E. C.; Shekhar, C.; Borrmann, H.; Stolz, S. et al. Controllable orbital angular momentum monopoles in chiral topological semimetals. *Nat. Phys.* **2024**, *20*, 1912–1918.
[56] Shcherbakov, D.; Stepanov, P.; Memaran, S.; Wang, Y. X.; Xin, Y.; Yang, J. W.; Wei, K. Y.; Baumbach, R.; Zheng, W. K.; Watanabe, K. et al. Layer- and gate-tunable spin-orbit coupling in a high-mobility few-layer semiconductor. *Sci. Adv.* **2021**, *7*, eabe2892.
[57] Sun, R.; Park, K. S.; Comstock, A. H.; McConnell, A.; Chen, Y. C.; Zhang, P.; Beratan, D.; You, W.; Hoffmann, A.; Yu, Z. G. et al. Inverse chirality-induced spin selectivity effect in chiral assemblies of π-conjugated polymers. *Nat. Mater.* **2024**, *23*, 782–789.